Applied Surface Science 520 (2020) 146326

Contents lists available at ScienceDirect

Applied Surface Science

journal homepage: www.elsevier.com/locate/apsusc

# β-$Ta_2O_5$ thin film for implant surface modification triggers superior anti-corrosion performance and cytocompatibility of titanium

Thamara Beline[a,b], Amanda B. de Almeida[a], Nilton F. Azevedo Neto[c], Adaias O. Matos[a,b], Antônio P. Ricomini-Filho[d], Cortino Sukotjo[e], Paul J.M. Smeets[f,g], José H.D. da Silva[c], Francisco H. Nociti Jr[a], Valentim A.R. Barão[a,b,*]

[a] University of Campinas (UNICAMP), Piracicaba Dental School, Department of Prosthodontics and Periodontics, Av. Limeira, 901, Piracicaba, São Paulo 13414-903, Brazil
[b] Institute of Biomaterials, Tribocorrosion and Nanomedicine (IBTN), Brazil
[c] São Paulo State University (UNESP), School of Sciences, Department of Physics, Av. Eng. Luís Edmundo C. Coube, 14-01, Bauru, São Paulo 17033-360, Brazil
[d] University of Campinas (UNICAMP), Piracicaba Dental School, Department of Physiological Science, Av. Limeira, 901, Piracicaba, São Paulo 13414-903, Brazil
[e] University of Illinois at Chicago, College of Dentistry, Department of Restorative Dentistry, 801 S. Paulina, Chicago, IL 60612, USA
[f] Department of Materials Science and Engineering, Northwestern University, Evanston, IL 60208, USA
[g] NUANCE Center, Northwestern University, Evanston, IL 60208, USA

ARTICLE INFO

*Keywords:*
Dental implants
Corrosion
Magnetron sputtering
Tantalum oxide
Protein adsorption
Biomaterials

ABSTRACT

In this study, β-tantalum oxide (β-$Ta_2O_5$) thin film was synthesized via magnetron sputtering to improve the surface properties, cytocompatibility and electrochemical stability of titanium. X-ray diffraction analysis confirmed a crystalline orthorhombic phase of $Ta_2O_5$ film on the β-$Ta_2O_5$ experimental surface. A granular structure with a complex and hierarchical nature was demonstrated by atomic force microscopy. $Ta_2O_5$-treated surfaces exhibited greater roughness and hydrophilicity compared with untreated titanium discs (control). Enhanced electrochemical stability in simulated body fluid (pH 7.4) was noted for $Ta_2O_5$-treated surfaces wherein higher values of charge transfer resistance, nobler corrosion potential, and lower capacitance, corrosion current density, and corrosion rate values were observed vs untreated control. Real-time monitoring of albumin and fibrinogen proteins adsorption by an electrochemical quartz crystal microbalance disclosed similar protein interactions for control and $Ta_2O_5$-treated discs, with higher fibrinogen adsorption rates for $Ta_2O_5$-treated surfaces. Cell culture assays (MC3T3-E1 cells) demonstrated that $Ta_2O_5$-treated discs featured greater *in vitro* mineral nodule formation, normal cell morphology and spreading, and increased mRNA levels of runt-related transcription factor 2 *(Runx-2)*, osteocalcin *(Ocn),* and collagen-1 *(Col-1)*. Therefore, it can be concluded that β-$Ta_2O_5$ thin films may be considered a promising strategy to trigger superior long-term stability and biological properties of titanium implants.

## 1. Introduction

Titanium (Ti) is one of the materials of choice as a permanent biomaterial, particularly for dental and orthopedic applications, due to its favorable characteristics related to mechanical strength, cytocompatibility, chemical stability, and corrosion resistance [1]. Ti is a highly reactive metal likely to undergo oxidation [1,2]. Thus, the formation, on Ti surfaces exposed to air or water, of a protective thin oxide layer consisting of titanium dioxide ($TiO_2$) provides corrosion resistance [3]. However, no metal or metal alloy is considered entirely inert in the biological environment [4], since the nature, thickness, and composition of the protective oxide layer on Ti surfaces may be affected by environmental conditions [5]. Previous studies have shown that the electrochemical behavior of Ti is negatively affected by exposure to saliva, fluorides, acid attack, microbial components, $H_2O_2$, nicotine, and metabolites from bacteria [6–13].

The corrosion process may result in ion release into the biological environment [14]. The presence of metal ions released from corrosion events is associated with peri-implant sites [15]. High amounts of dissolved Ti around implants with peri-implantitis were found when compared with healthy implants [15], revealing that Ti ion release from implant surfaces during the corrosion process is linked to peri-

* Corresponding author at: University of Campinas (UNICAMP), Piracicaba Dental School, Department of Prosthodontics and Periodontics, Av. Limeira, 901, Piracicaba, São Paulo 13414-903, Brazil.
*E-mail address:* vbarao@unicamp.br (V.A.R. Barão).

https://doi.org/10.1016/j.apsusc.2020.146326
Received 21 October 2019; Received in revised form 28 March 2020; Accepted 6 April 2020
Available online 14 April 2020
0169-4332/ 

implantitis. In addition, the corrosion of Ti may affect its resistance to fatigue, compromising implant mechanical stability [16] and leading to treatment failure. Such facts emphasize the need for the development of alternative materials.

In this framework, tantalum (Ta) has attracted attention as a new alternative biomaterial because of its high bioactivity and superior corrosion resistance compared with that of Ti in harsh environments [17,18]. Such good cytocompatibility and corrosion resistance of Ta can be associated with the formation of a high-stability, self-passivating tantalum pentoxide ($Ta_2O_5$) on the surface [19]. However, in the form of a bulk material, the high cost and density of Ta implants restrict their use. Moreover, another issue to be considered relative to its use as a biomedical device is the high melting temperature of bulk Ta (~3017 °C) [18]. Therefore, Ta and $Ta_2O_5$ coatings have been deposited on different materials to improve their surface properties. The biocompatibility, bioinertness, corrosion and abrasion resistance makes $Ta_2O_5$ a suitable alternative for using as a protective coating in biomedical devices [20–22]. Despite presenting the aforementioned characteristics, pure Ta coatings do not have satisfactory wear resistance [23].

Among all the methods available for the deposition of $Ta_2O_5$ films [18,24], magnetron sputtering is a versatile technique well-known to produce uniform film growth and films with excellent adhesion to the substrate [25], which makes this technique interesting in terms of corrosion protection. Additionally, the films can be deposited at relatively high purity and low cost [26]. Our previous study tailored the deposition parameters of magnetron sputtering to synthesize $Ta_xO_y$ films onto commercially pure titanium (cpTi) surfaces [27]. A crystalline β-$Ta_2O_5$ film appears to be more suitable for biomedical applications [27]. However, there is limited understanding of the chemical degradation of β-$Ta_2O_5$ films in simulated oral conditions. Additionally, no study has evaluated real-time protein/β-$Ta_2O_5$ film interactions, which is crucial since protein adsorption is one of the first biological responses in the human body to trigger a manifold of biological processes [28].

Thus, to improve the electrochemical stability and cytocompatibility of cpTi, we deposited $Ta_2O_5$ films onto cpTi surfaces by means of a magnetron reactive sputtering deposition technique. The aims of this study were (1) to characterize the physical and chemical properties of the $Ta_2O_5$ film, (2) to evaluate the role of the $Ta_2O_5$ film in the electrochemical behavior of cpTi, (3) to investigate the real-time adsorption of albumin and fibrinogen onto the cpTi surfaces, and (4) to evaluate the cellular responses and gene expression of pre-osteoblastic cells (MC3T3-E1) cultured on modified cpTi surfaces.

## 2. Materials and methods

### 2.1. Sample preparation

CpTi grade II samples, 2 mm in thickness and 15 mm in diameter (Mac-Master Carr, USA) were ground with SiC grinding paper (#320, #400, and #600) (Carbimet 2; Buehler, USA), and polished initially using a polishing cloth (Satyn MB; Buehler) with a 9-μm aqueous polycrystalline diamond suspension (MetaDi Supreme; Buehler) and subsequently with colloidal silica suspension and polishing disc (Chemio MB; Buehler). Finally, samples were cleaned in an ultrasonic bath with deionized water (10 min), acetone (10 min), and isopropyl alcohol (10 min) and air-dried.

### 2.2. Deposition of $Ta_2O_5$ films by magnetron sputtering

A radiofrequency (RF) magnetron sputtering system (Kurt J. Lesker Company, USA) was used for $Ta_2O_5$ films deposition. The deposition was conducted in an Ar + $O_2$ atmosphere ($Ar/O_2$ ratio = 2.5). Before each deposition process, the metallic Ta target (3″ in diameter and 99.95% purity) (Kurt J. Lesker Company) surface was plasma cleaned during 5 min in an Ar atmosphere at $7.5 \times 10^{-3}$ Torr and 100 W power to eliminate contaminants from the target surface. Base pressure lower than $5.0 \times 10^{-6}$ Torr was considered appropriate to initiate the deposition in the chamber [29]. Next, the oxide films were deposited on heated cpTi discs and on quartz slabs in separate deposition cycles. While Ti substrates were heated at 600 °C, the quartz slabs used in the quartz crystal monitor were heated at 500 °C. According to the manufacturer, the quartz crystal slabs must be subjected to temperatures below 532 °C in order to prevent deterioration of the piezoelectric properties. A K-type thermocouple wire was used for substrate temperature measurements during the deposition. The deposition parameters used were based on results from our previous study [27]. The atmosphere was composed of $O_2$ (8 sccm) and Ar (20 sccm), the bias voltage and the process power were kept constant at −164 V and 400 W RF, while the working pressure was $6.0 \times 10^{-3}$ Torr. The deposition process was conducted for 67 min.

### 2.3. Surface characterization

#### 2.3.1. X-ray diffraction (XRD) analysis

X-ray diffractometry (XRD - X'Pert$^3$ PRO MRD; PANalytical, The Netherlands) was used to investigate the structural properties of the film, with a θ–2θ configuration in the 20–80° range with a step size of 0.01° and CuKα (λ = 1.54056 Å) radiation.

#### 2.3.2. Atomic force microscopy (AFM)

AFM (Park NX10; Park System, USA) analysis was performed to evaluate the 3D surface topography of different cpTi surfaces. Images of 5 μm × 5 μm were obtained in tapping mode with a constant force and frequency of 42 N/m and 320 kHz, respectively. Two different areas were used to obtain the roughness (Ra) values, and Gwyddion software (GNU General Public License, Czech Republic) was used to calculate the estimated surface area of the samples.

#### 2.3.3. Surface energy

Surface energy measurements were performed using a goniometer (Ramé-Hart 100–00; Ramé-Hart Instrument Co., USA) which included deionized water (polar component) and diiodomethane (dispersive component) (2 μL), following the previous protocol suggested by Combe et al. [30]. To ensure reproducibility, the test was conducted at least five times.

#### 2.3.4. X-ray photoelectron spectroscopy (XPS)

To obtain the chemical composition of the oxide layer of cpTi and $Ta_2O_5$ substrates, XPS analysis was carried out. A spectrometer (K-Alpha X-ray XPS; Thermo Scientific, Finland) with a hemispheric analyzer was operated with energy step at 0.100 eV and spot size at 400 μm [6].

#### 2.3.5. Cross-sectional analysis using a focused ion beam-scanning electron microscope (FIB-SEM)

A polished cpTi disc including the deposited magnetron sputtered $Ta_2O_5$ film was affixed onto a 45° aluminum SEM pin stub specimen mount (Ted Pella, Inc., USA) using double-sided conductive carbon tape. A dual-beam FIB-SEM (FEI Helios Nanolab 600; Thermo Fisher Scientific, USA) with a gallium liquid metal ion source (LMIS) operating at an accelerating voltage of 30 kV was used to prepare cross-sections of the $Ta_2O_5$ film and underlying Ti substrate. At the center of the disc, primarily a ~50 nm layer of protective platinum was deposited on a 2 μm × 20 μm (length × width) area of interest using the electron beam (5 kV, 1.4nA) through decomposition of a (methylcyclopentadienyl)-trimethyl platinum precursor gas (FEI Helios Nanolab 600; Thermo Fisher Scientific). Directly on top of this, a ~1.0 μm thick protective platinum layer was deposited using the ion beam (30 kV, 93 pA) through decomposition of the same precursor gas. Subsequently, a several micrometer deep trench was cut directly adjacent to the area of

interest using the ion beam. Next, the cross-section was cleaned up at a voltage of 30 kV and a current of 0.92nA until approximately halfway down the length of the area of interest. The sample was then tilted to observe the cross-section using the electron beam at an incident angle of 45° using an Elstar UHR immersion lens for high resolution imaging. The final thickness assessment of the $Ta_2O_5$ layer was performed using line profiles (taking into account the appropriate tilt correction) using the xT microscope Control software (FEI Helios Nanolab 600; Thermo Fisher Scientific).

### 2.4. Electrochemical assay

A potentiostat (Interface 1000; Gamry Instruments, USA) was used for the corrosion assessment. A three-electrode cell standardized method was used in conformity with the American Society for Testing of Materials (G61 86 and G31 72). The exposed surface of cpTi sample was used as the working electrode, a graphite rod as the counter electrode and a saturated calomel electrode (SCE) as the reference electrode. AFM analysis was performed to estimate the exposed surface area of the two groups (cpTi = 1.77 $cm^2$; $Ta_2O_5$ = 7.06 $cm^2$). For the simulation of the oral conditions (blood plasma), simulated body fluid (SBF) was used at 37° C and pH 7.4 as electrolyte solution [31]. Prior to the tests, a cathodic potential (-0.9 V vs SCE) was applied for 600 s. Subsequently, the Open Circuit Potential (OCP) was scanned for 3600 s followed by the electrochemical impedance spectroscopy (EIS) measurements [32]. Such data were used to estimate the real ($Z_{real}$) and imaginary ($Z_{imag}$) components of the impedance, which were presented as Nyquist plot, impedance (|Z|) and phase angle [6]. For quantifying the electrochemical kinetics, including corrosion resistance ($R_p$), charge transfer resistance ($R_{ct}$), and constant phase element ($Q_{dl}$), an equivalent electrical circuit was used. Subsequently, the polarization of the specimens were conducted from −0.8 V to 1.8 V (2 mV/s scan rate) [33,34]. A Tafel extrapolation method was used to determine the polarization curves, which provided the electrochemical variables corrosion potential ($E_{corr}$), corrosion current density ($I_{corr}$), and corrosion rate. All measurements were performed at least five times to guarantee reproducibility and reliability.

### 2.5. Biological assessments

#### 2.5.1. Real-time monitoring of protein adsorption by EQCM

To understand how the proteins interacted with the modified Ti surfaces, we monitored the adsorption of albumin and fibrinogen using the EQCM device (eQCM 10 M; Gamry Instruments). For this purpose, a 5 MHz quartz crystal (Gamry Instruments) covered with Ti (control) and a 5 MHz quartz crystal treated with a $Ta_2O_5$ film (experimental) were used. To ensure reproducibility, the tests were performed at least three times. Prior to the tests, the quartz crystal specimens were carefully cleaned with copious deionized water and propanol, and subsequently air-dried. The albumin (Sigma–Aldrich, USA) solution was prepared by dissolution in phosphate-buffered saline (PBS) (Gibco, Life Technologies, USA) (1 mg/mL). Fibrinogen (Sigma–Aldrich) solution was produced by dissolution in 0.9% NaCl (1 mg/mL). The quartz crystal sample was coupled in the EQCM device containing 6.5 mL of PBS or 0.9% NaCl, depending on the protein used in the test. After 30 min (1800 s) of system stabilization, a 500-µL quantity of albumin or fibrinogen solution was inserted into the system, and the real-time protein adsorption kinetic was monitored for 2 h and 30 min by means of Gamry Resonator software (Gamry Instruments) at ambient temperature (25 °C). The QCM frequency shifts ($\Delta f_s$) were related to the mass change ($\Delta M$) per unit area on the surface of the working electrode (quartz crystal) according to the Sauerbrey equation [35]:

$$\Delta f_s = \frac{-2nf_1^2 \Delta M}{Z_q}$$

where $n$ is the order of the measured harmonic (3), $f_1$ is the fundamental frequency (5 MHz) and $Z_q$ is the theoretical acoustic impedance of quartz ($8.84 \times 10^6$ kg $m^{-2}$ $s^{-1}$). Thus, the adsorption of protein was calculated by means of the $\Delta M$ on the quartz crystal surface as a function of time. Then, the following variables were calculated: $\Delta M$ (µg), adsorption rate (ng/s), mass loss (µg), and effective mass gain (µg). For the calculation of $\Delta M$ (µg), the maximum value of protein adsorption reached during the test was subtracted from the adsorption value obtained at 1800 s (point of final stabilization of the system, when the protein was inserted). The adsorption rate (ng/s) was determined by means of the division of $\Delta M$ by the difference between the initial time (1800 s) and the time where the maximum adsorption value was reached during the test. The mass loss was estimated by the difference between the maximum adsorption value and the adsorption value at the end of the analysis (10,800 s). Finally, the effective mass gain (µg) was determined by the difference between $\Delta M$ and mass loss values.

#### 2.5.2. Cell culture

Pre-osteoblastic MC3T3-E1 cells were cultivated in Alpha MEM (Gibco, Life Technologies, USA) supplemented with penicillin (100 U/mL), streptomycin (100 mg/mL) and 10% fetal bovine serum (FBS) (Gibco), at 5% $CO_2$ atmosphere conditions and 37 °C. After reaching confluence, trypsin-ethylenediaminetetraacetic acid (Gibco) was used to detach the cells. Next, the cells were re-suspended in culture medium for seeding onto the samples.

#### 2.5.3. MTT assay

Cellular metabolic activity on experimental and control surfaces was determined at 1, 2, and 4 days by MTT 3-(4,5-dimethylthiazol-2-yl)-2,5-diphenyltetrazolium bromide analysis. After the experimental periods, the culture medium was replaced by α-MEM with MTT (5 mg/mL) (Gibco) at 37 °C and 5% $CO_2$ atmosphere conditions for 4 h following the manufacturer's recommendation. Subsequently, dimethyl sulfoxide (Sigma-Aldrich) was used to dissolve the formazan crystals. Next, the optical density was verified (VersaMax; Molecular Devices, USA) at a 570 nm wavelength [36]. The tests were performed in triplicate to guarantee reproducibility.

#### 2.5.4. Scanning electron microscopy (SEM) analysis

To analyze the effects of untreated control and experimental surfaces on cell morphology, pre-osteoblastic MC3T3-E1 cells were plated in duplicate at $1.5 \times 10^4$ cells/mL in 24-well culture plates containing α-MEM supplemented with antibiotics and 10% FBS, for 24 h in order to allow cell adhesion onto the specimen surface. Next, the medium was replaced by α-MEM supplemented with antibiotics plus 2% FBS (day 0), which was replaced daily until the end of each experimental period. Cell morphology and spreading were verified by SEM analysis after 1, 2, and 4 days. Briefly, cells were fixed with Karnovsky's solution at 4 °C for 12 h and subsequently fixed in 1% osmium tetroxide for 1 h at room temperature. Next, cells were dehydrated in ethanol (35, 50, 70, 90, and 100%) at 25 °C for 10 min, critical-point dried (mod. DCP-1; Denton Vacuum, USA) and sputtered with gold (mod. SCD 050; Bal-Tec, USA) [27,37].

#### 2.5.5. Fluorescence analysis

The cell morphology was further determined by confocal imaging (LSM 800; Carl Zeiss, Germany) after 1 and 2 days. For confocal imaging, MC3T3-E1 cells were plated at a density of $1.5 \times 10^4$ cells/mL in 24-well cell culture plates, washed in PBS, fixed for 30 min with 4% formaldehyde, and permeabilized for 10 min in 0.01% Triton X100 in PBS. ActinRed™ 555 ReadyProbes® Reagent (Molecular Probes, USA) was used for the cell cytoskeleton staining (25 min), and Hoechst (Thermo Fisher Scientific, USA) for the nucleus staining (10 min). The specimens were then twice washed in PBS before undergoing confocal microscopic analysis.

#### 2.5.6. Mineralization analysis by Alizarin red staining

Mineral nodule formation was quantitatively assessed by the Alizarin Red assay at 4, 7, and 14 days of incubation in Alpha MEM plus antibiotics either supplemented with or without 100 nM dexamethasone, 0.05 mM L-ascorbic acid and 10 mM β-glycerophosphate disodium salt hydrate, allowing osteoblastic cell differentiation in an atmosphere of 5% $CO_2$ and 37 °C conditions. After the experimental periods, the fixation process of the cells in 70% ethanol was conducted for 60 min. NanoPure water (resistivity of 18.2 MΩ.cm at 25 °C) was used to remove the ethanol and next, the cells were stained with Alizarin Red solution (AR-S) at 37 °C for 10 min. Subsequently, cells were immersed five times in NanoPure solution to remove the AR-S not bound to the cells/matrix, and a 600-μL quantity of PBS was added to each well under stirring for 15 min to reduce non-specific staining. Next, cetylpyridinium chloride at 10% was used to maximize the elution of AR-S staining for 30 min. Finally, a 100-μL quantity of the solution from each sample was transferred to a 96-well plate in triplicate for the absorbance reading of the solution by spectrophotometry (562 nm) [38]. To ensure reliability, the tests were performed in triplicate.

#### 2.5.7. Quantitative reverse transcriptase real-time polymerase chain reaction analysis (RT-qPCR)

To analyze mRNA levels of osteogenic markers, we cultured pre-osteoblastic MC3T3-E1 cells onto untreated control and modified cpTi discs and analyzed qPCR reactions. Cells were cultured for 1, 2, and 3 days in an α-MEM supplemented with 100 nM dexamethasone, 0.05 mM L-ascorbic acid and 10 mM β-glycerophosphate disodium salt hydrate, allowing osteoblastic cell differentiation. Total RNA was obtained by means of RNeasy Plus Mini Kit (Qiagen Sciences, USA), a commercially available system as recommended by the manufacturer. RNA concentration and quality were assessed by spectrophotometry (Nanodrop 1000; Thermo Scientific), and cDNA was obtained by means of a RT2 First Strand Kit for reverse transcription polymerase chain reaction (Qiagen Sciences). qPCR reactions were performed by means of the FastStart Universal SYBR Green Master (Roche Diagnostics GmbH, Germany) and LightCycler® 480 instrument (Roche Diagnostics GmbH). Transcript levels for runt-related transcription factor 2 (*Runx-2*), alkaline phosphatase (*Alpl*), osteocalcin (*Ocn*), and Collagen-1 (*Col-1*) were obtained and normalized by β-actin mRNA levels (Table 1). All the tests were performed in triplicate.

#### 2.5.8. Bioactivity test

For the bioactivity test, untreated control and experimental surfaces were immersed in SBF solution at 37 °C for 14 days in a plastic tube following the protocol suggested by Kokubo *et al.* [39]. The volume of SBF was estimated in agreement with the following formula: $V_{SBF} = S_a/10$, where $V_{SBF}$ is the volume of SBF (unit: mL) and $S_a$ is the surface area of the specimen (unit:$mm^2$). After 14 days, the discs were washed with distilled water and air dried. The XRD test was conducted to investigate the presence of apatite crystals on the specimen [39].

**Table 1**
Primer sequences for the assessed genes.

| Genes | | Primer Sequences (3′ to 5′) |
|---|---|---|
| *Runx-2* | Forward | *cgtgtcagcaaagcttctttt* |
| | Reverse | *ggctcacgtcgctcatct* |
| *Alpl* | Forward | *ggggacatgcagtatgagtt* |
| | Reverse | *ggcctggtagttgttgtgag* |
| *Ocn* | Forward | *tgaacagactccggcg* |
| | Reverse | *gataccgtagatgcgtttg* |
| *Col-1* | Forward | *gagggccaagacgaagacatc* |
| | Reverse | *cagatcacgtcatcgcacaac* |
| *β-actin* | Forward | *ctaaggccaaccgtgaaaag* |
| | Reverse | *accagaggcatacagggaca* |

### 2.6. Statistical analysis

IBM SPSS Statistics for Windows (IBM SPSS Statistics for Windows, v.21.0, IBM Corp., USA) was used to evaluate the data. The comparison of surface roughness, surface energy, corrosion data ($R_p/R_{ct}$, Q, $E_{corr}$, $I_{corr}$, and corrosion rate), EQCM data ($\Delta M$, adsorption rate, mass loss, and effective mass gain) between cpTi and $Ta_2O_5$-coated samples were conducted with an independent *t*-test. A 2-way ANOVA test (factor 1, surface type in 2 levels; factor 2, days in 3 levels) and the Tukey Honestly Significant Difference (HSD) test for post hoc comparisons were used to analyze the cell metabolism (MTT) data. Calcium ion concentration results were evaluated with 3-way ANOVA (factor 1, surface type in 2 levels; factor 2, days in 3 levels; factor 3, culture medium conditions in 2 levels) for investigation of the impact of surface treatment, days, and non-osteogenic (control) or osteogenic medium conditions and their interaction on calcium ion concentration levels. The Tukey HSD test was used as a post hoc technique when needed. For qRT-PCR test, data were analyzed by Kruskal-Wallis test for investigation of the influence of the surface treatment on *Runx-2*, *Alpl*, *Ocn* and *Col-1* expression. To compare the groups in pairs, the Mann-Whitney *U* test was used ($r > 0.82$). The p value, which is defined as the probability of observing the given value of the statistic test, or greater, under the null hypothesis, was considered statistically significant when $< 0.05$. This guarantee that the probability of error is below 5%.

## 3. Results and discussion

### 3.1. Structural analysis, surface topography, and surface energy

The X-ray diffraction patterns of control (cpTi substrate) and experimental ($Ta_2O_5$) groups are displayed in Fig. 1. Both groups presented diffraction peaks equivalent to metallic Ti. Such behavior is explained due to the penetration depth of Cu-$K_\alpha$ radiation (~10 μm), which is higher than the film thickness (~600 nm) [40]. Additionally, the diffraction peaks at 27.5°, 49.0° and 70.6° found in the $Ta_2O_5$ group appoint to the presence of the crystalline orthorhombic structure of the $Ta_2O_5$ film (ICDD cards numbers 89–2843 and 79–1375), which can also be referred to as β-$Ta_2O_5$ [41].

The surface topography is well known for playing an essential role in cytocompatibility, being considered crucial for biological applications [42]. The morphology and topography of the cpTi substrate and the $Ta_2O_5$ film deposited on cpTi surfaces obtained from AFM analysis are shown in Fig. 2. The surface treatment with $Ta_2O_5$ films evidently modified the surface topography of the cpTi substrates, showing a granular structure with a complex and hierarchical nature. In contrast,

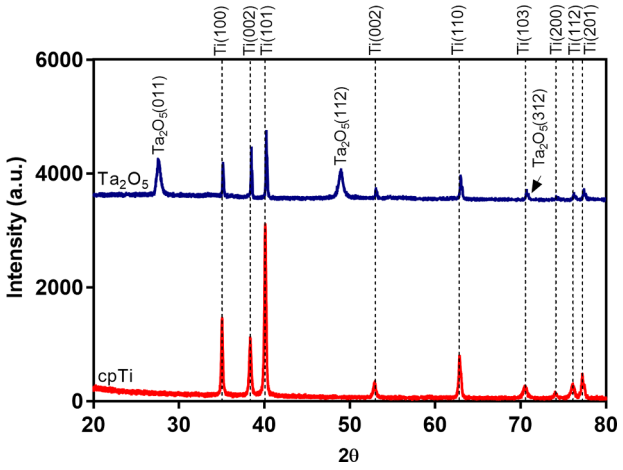


**Fig. 1.** X-ray diffraction patterns obtained from the cpTi substrate (red pattern) and the $Ta_2O_5$ film deposited on cpTi surfaces (blue pattern).

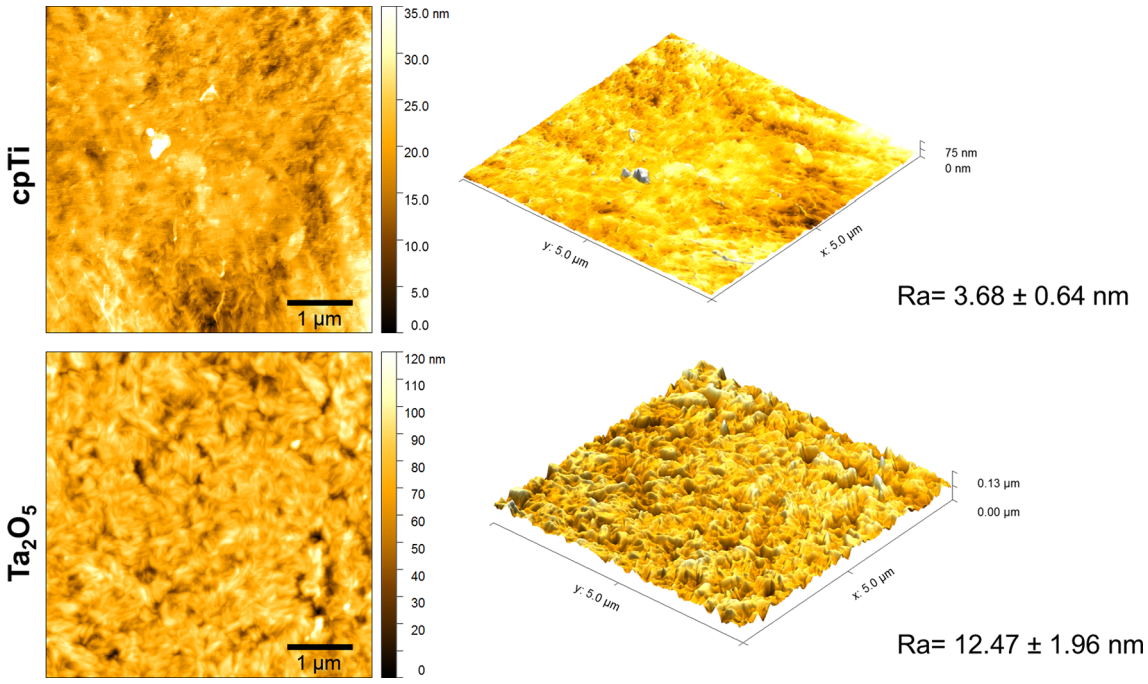


**Fig. 2.** AFM 2D and 3D images obtained from the cpTi substrate and $Ta_2O_5$ film deposited on cpTi surfaces (scale bar = 1 µm).

the polished cpTi group exhibited smooth and flat surfaces. In the 3D profile, a greater Ra value (mean ± standard deviation) can be observed for the $Ta_2O_5$ group (Ra = 12.47 ± 1.96 nm), while the control group exhibited the lowest value (Ra = 3.68 ± 0.64 nm). It has been showed that cell adhesion was significantly improved in surfaces with nanoscale patterns when compared with cells cultivated on surfaces with microscale patterns [43].

In addition to surface roughness, another important factor with respect to the surface properties of a biomaterial is surface energy, which controls the contact area of the substrate with the cell membrane [44]. Fig. 3 shows the surface energy values for all groups. Higher surface energy values were found for the $Ta_2O_5$ group when compared with cpTi, which indicates a hydrophilic tendency of the $Ta_2O_5$ group. It was reported that hydrophilic surfaces positively impact on the attachment and spreading of osteoblasts [45].

### 3.2. Surface chemistry characterization

Fig. 4 shows the high-resolution spectra of control and $Ta_2O_5$ groups obtained from XPS analysis. In the Ti 2p spectrum, doublets can be seen at 464.70 and 459.20 eV, corresponding to the Ti $2p_{1/2}$ and Ti $2p_{3/2}$ bands, respectively (Fig. 4a). These peaks values are related to $TiO_2$ [46,47]. The energy peaks found in the O 1s spectrum of the control group (Fig. 4b) also correspond to $TiO_2$. In the Ta 4f spectrum (Fig. 4c), the energy peaks found are related to the formation of $Ta_2O_5$, corroborating results from previous studies [48,49]. Two peaks can be observed in the O 1s spectrum of the $Ta_2O_5$ group (Fig. 4d), wherein the 530.00 eV energy is appointed to Ta-O binding, constituting tantalum oxides [49,50], and the binding energy of 531.90 eV is related to oxygen in the form of a hydroxide or to adsorbed oxygen species [49,51].

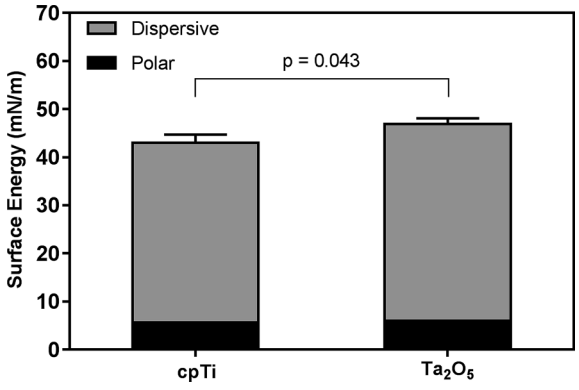


**Fig. 3.** Surface energy for control cpTi and $Ta_2O_5$ surfaces. Intergroup difference (cpTi vs $Ta_2O_5$) is illustrated by the p-value.

Cross-sectional analysis of the$Ta_2O_5$ thin film deposited onto the cpTi substrate by means of FIB-SEM is shown in Fig. 5. The film appears homogeneously deposited and compact (Fig. 5), with rarely displaying some pores in between the substrate and film (Fig. S1). The film thickness was measured to be approximately 600 nm.

### 3.3. Surface electrochemistry characterization

The evolution of OCP as a function of time (s) for the cpTi substrate and the cpTi covered with the $Ta_2O_5$ film is shown in Fig. 6. The $Ta_2O_5$ group showed the most positive values of OCP compared with the control group. It is known that better corrosion behavior is associated with more positive OCP values. Considering this, these data may appoint to improvement of the electrochemical resistance of the $Ta_2O_5$ surface treatment.

The Nyquist plot represents the evolution of resultant impedance as a function of $Z_{real}$ and $Z_{imag}$ components (Fig. 7a). It has been well-established that a decrease in the diameter of the semicircular loop indicates a reduction in passive film resistance [52]. The control group exhibited a decrease in the semicircular diameter (on the order of $10^5$). For the $Ta_2O_5$ group, the semicircular diameter of the capacitance loop was on the order of $10^8$, indicating improved corrosion resistance. The variation in impedance as a function of frequency was provided by Bode plots (Fig. 7b). Greater total impedance values can be seen for $Ta_2O_5$-treated surfaces. Such behavior indicates that this group has superior electrochemical resistance, since high impedance values at low frequencies suggest the formation of a highly stable oxide film on the surface. The phase angles of the $Ta_2O_5$-coated samples are slightly higher than those observed for cpTi samples (Fig. 7c), indicating an

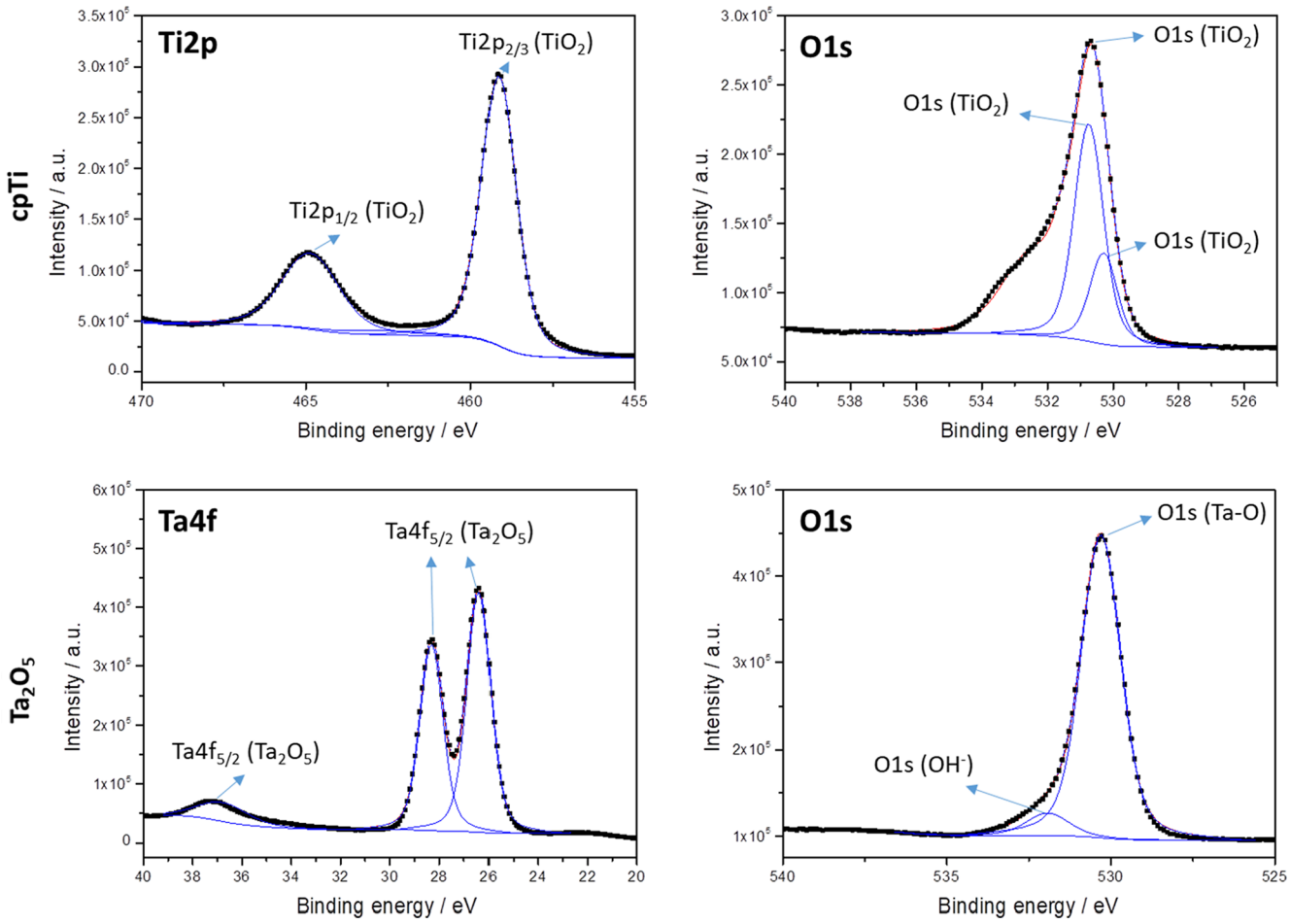


**Fig. 4.** X-ray photoelectron spectroscopy (XPS) spectra of (a) Ti2p and (b) O1s for the control cpTi substrate and (c) Ta4f and (d) O1s for the $Ta_2O_5$ film deposited on cpTi surfaces.

improvement of the electrochemical stability of cpTi when subjected to this treatment. In addition, it is possible to observe that both groups exhibited only one time constant. The equivalent electrical circuit used for the simulation of the electrical parameters of the surfaces is illustrated in Fig. 7d. The values of chi-square ($\chi^2$) were on the order of $10^{-3}$–$10^{-4}$, indicating that the fitted data are in accordance with the experimental data. In the simplified circuit, $R_s$ corresponds to the resistance of the solution between the reference and working electrodes, $Q_{dl}$ is considered as the constant phase element (CPE) attributed to the electrical double layer, $R_p$ is the resistance of the passive film (control group), and $R_{ct}$ is the charge transfer resistance (experimental group). The use of this circuit was based on results from previous studies

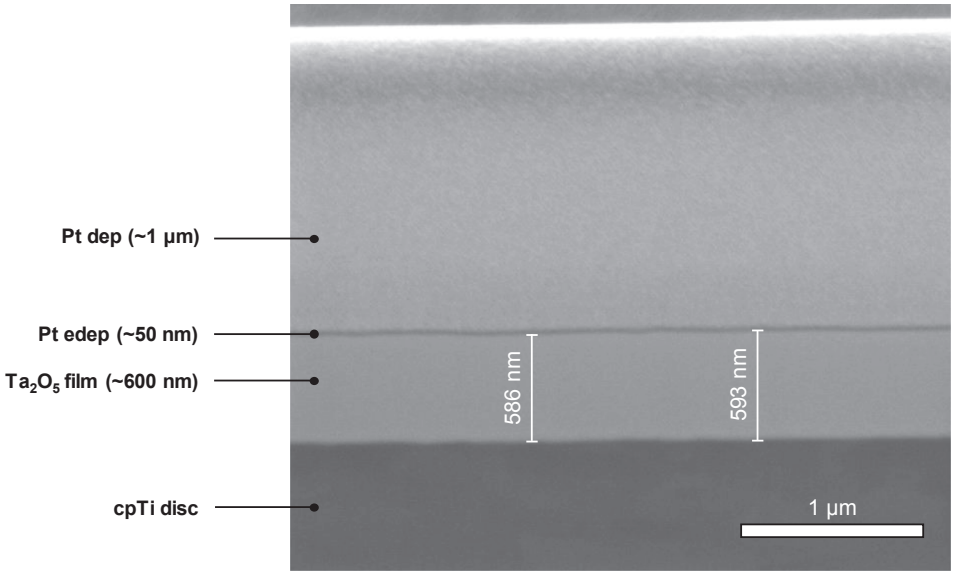


**Fig. 5.** Cross-sectional FIB-SEM micrograph of the $Ta_2O_5$ thin film deposited onto the cpTi substrate. Platinum (Pt) was deposited on the cross-section area of interest initially using the electron beam (Pt edep) and subsequently using the ion beam (Pt dep) to protect the film from exposure to the ion beam during cross-sectional milling.

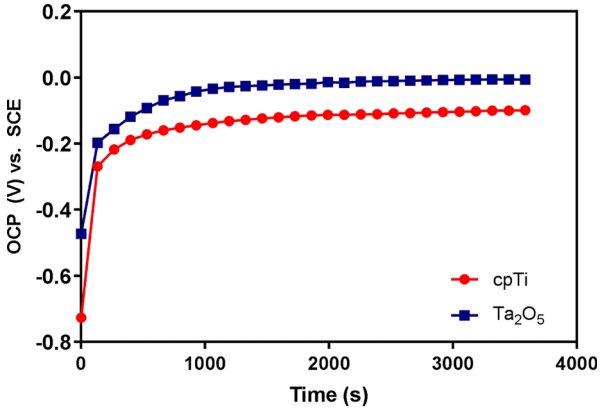


**Fig. 6.** Representative curve of OCP evolution (in V vs SCE) for control cpTi (red curve) and $Ta_2O_5$ (blue curve) surfaces exposed to SBF solution for 3600 s.

[49,53].

The OCP, Nyquist, and impedance data corroborates with the results of the electrochemical parameters obtained from EIS (Table 2). Higher values of resistance can be seen for the $Ta_2O_5$ film, while cpTi exhibited the lowest resistance values. This behavior suggests that the surface treatment is able to provide better protection against corrosion. In contrast, cpTi presented the greatest values of $Q_{dl}$, corroborating the corrosion resistance results. This fact supports the disadvantageous electrochemical properties of cpTi when it is exposed to SBF immersion, since higher capacitance values indicate an increase in the ionic exchange between the material and the electrolyte [6].

In the polarization curves (Fig. 8), it is possible to observe that the $Ta_2O_5$ group shifted the current density to lower values. When compared with the cpTi group, $Ta_2O_5$ shifted the curve to the upper left region of the graph, shifting the electrode potential to more positive values, which suggests a less active behavior in ion exchange of the $Ta_2O_5$ surface compared with cpTi.

The electrochemical parameters including $E_{corr}$, $I_{corr}$, and corrosion rate are described in Table 3. $I_{corr}$ is an electrochemical parameter that indicates the current flow at an open circuit potential as a result of oxidation or reduction reactions [54]. The results show that the $Ta_2O_5$ group exhibited lower $I_{corr}$ and corrosion rate values. Such findings demonstrate that the $Ta_2O_5$ film deposited on cpTi surfaces provides more efficient corrosion protection for the cpTi surface, confirming its favorable electrochemical properties. Additionally, more positive/nobler $E_{corr}$ values were observed for the$Ta_2O_5$ group when compared with the cpTi group.

The mechanism of the high corrosion protection of the $Ta_2O_5$ film may be related to its characteristics of high homogeneity and compactness as can be seen from the FIB-SEM cross-sectional analysis (Fig. 5). Such characteristics may help to reduce the penetration of ionic species through the film, leading to the mitigation of the electrochemical degradation process, explaining the excellent anti-corrosion performance of the $Ta_2O_5$ thin film.

### 3.4. Real-time interplay between protein and biomaterial

The subsequent cell-biomaterial interactions are mediated by protein adsorption. The human body contains thousands of proteins, with each protein performing a set of distinct and crucial functions, essentially since they have the ability to bind to specific molecules [55]. Albumin is the most predominant protein found in blood serum (~60%)

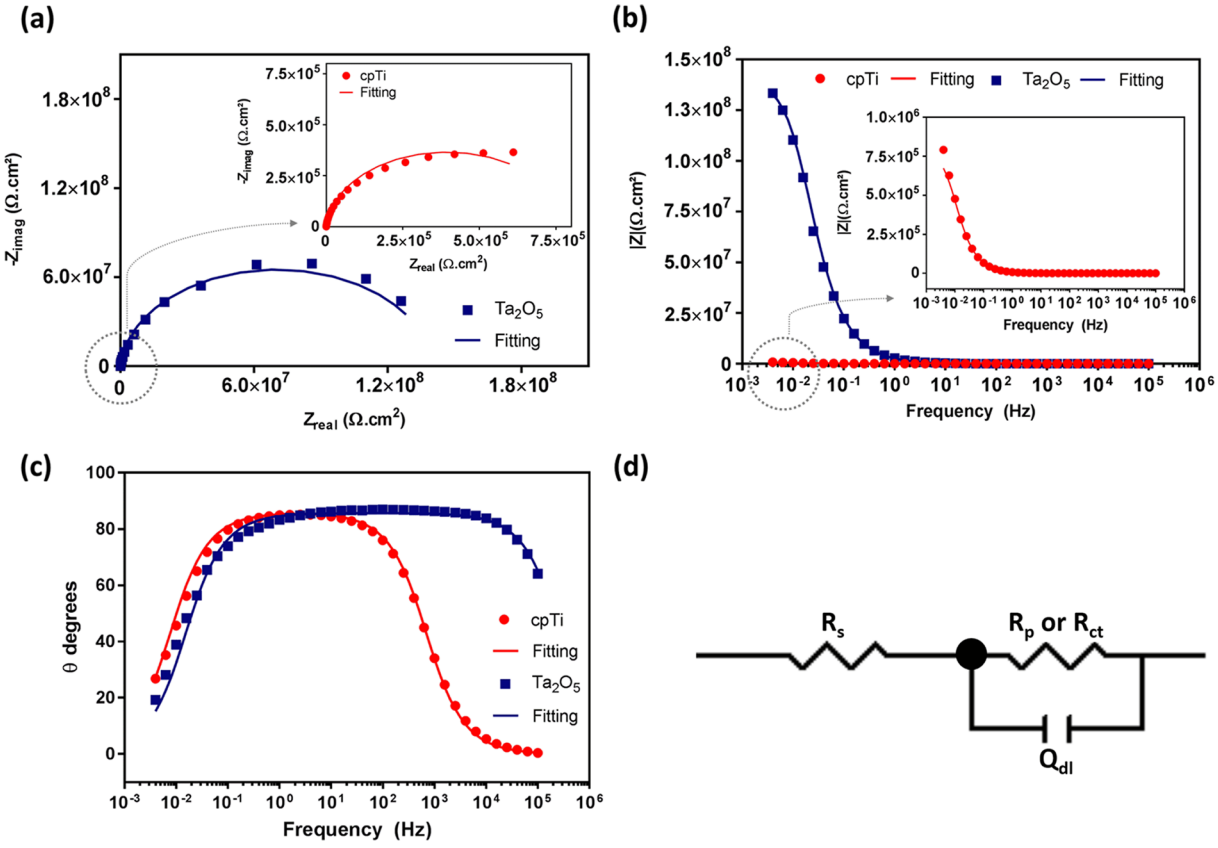


**Fig. 7.** Representative (a) Nyquist diagrams, (b) impedance modulus, and (c) phase angles of EIS responses for control cpTi (red curves) and $Ta_2O_5$ (blue curves) surfaces. Symbols represent experimental data and solid lines fitted data. Magnified graphs were plotted for better visualization. (d) Equivalent circuit used for EIS data, which shows resistance of solution ($R_s$) in series with a parallel combination of the constant phase element ($Q_{dl}$) and a charge transfer resistance ($R_{ct}$) or polarization resistance ($R_p$) of the oxide layer.

**Table 2**
Means (and standard deviations) of electrical parameters obtained from the equivalent circuit model for control cpTi and $Ta_2O_5$ surfaces.

| Group | $R_p$ or $R_{ct}$ (Mohms.cm$^2$) | $Q_{dl}$ (n$\Omega^{-1}$ S$^n$.cm$^{-2}$) | n | $\chi^2 \times 10^{-3}$ |
|---|---|---|---|---|
| cpTi | 1.79 (0.35)[a] | 12451.98 (1777.77)[a] | 0.95 (0.01) | 1.57 (1.10) |
| $Ta_2O_5$ | 1385.34 (646.64)[b] | 11.14 (3.57)[b] | 0.94 (0.03) | 3.38 (0.35) |

Note: Intergroup difference (cpTi vs $Ta_2O_5$) is illustrated by the different lower-case letters. $R_p$ is the resistance of the passive film (control cpTi group), and $R_{ct}$ is the charge transfer resistance ($Ta_2O_5$ experimental group).

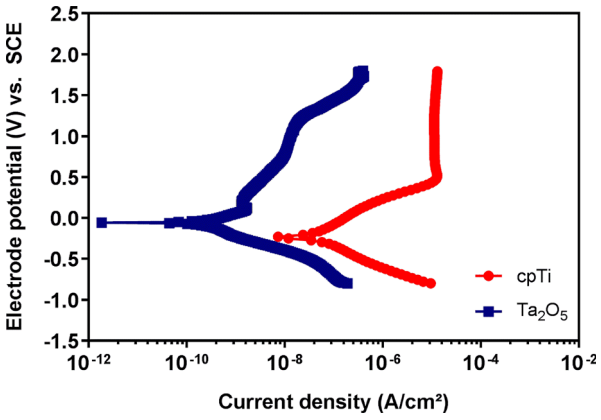


**Fig. 8.** Representative potentiodynamic polarization curves of control cpTi (red curve) and $Ta_2O_5$ (blue curve) surfaces. The electrode potential is expressed in V vs the saturated calomel electrode (SCE).

**Table 3**
Mean (and standard deviation) values of electrochemical parameters obtained from the potentiodynamic polarization curves for control cpTi and $Ta_2O_5$ surfaces.

| Group | $E_{corr}$ (mV) | $I_{corr}$ (nA/cm$^2$) | Corrosion rate (mpy) $\times 10^{-4}$ |
|---|---|---|---|
| cpTi | −206.15 (26.21)[a] | 21.93 (3.27)[a] | 131.52 (63.65)[a] |
| $Ta_2O_5$ | −14.01 (5.86)[b] | 0.44 (0.27)[b] | 2.05 (1.27)[b] |

Note: Intergroup difference (cpTi vs $Ta_2O_5$) is illustrated by the different lower-case letters.

[56]. Because of its high concentration in blood plasma, albumin is extensively used in protein adsorption studies [55]. Another important protein is fibrinogen, an abundant glycoprotein in blood plasma, involved in the blood coagulation process [55,57]. The previous literature demonstrated that fibrinogen is associated to the promotion of cell adhesion *in vitro* [57,58]. It was found that the adsorption of fibrinogen can contribute to fibrin formation, enhancing platelet adhesion [57]. In this study, we investigated the adsorption kinetics of albumin and fibrinogen onto Ti and $Ta_2O_5$ surfaces in real time using EQCM. The quantitative EQCM results showed similar protein interactions with Ti and $Ta_2O_5$ surfaces (Table 4). Fig. 9 shows the changes in $\Delta f_s$ and $\Delta M$ as a function of time during the adsorption processes of (a-b) albumin and (c-d) fibrinogen on quartz crystal sensors covered with Ti and treated with $Ta_2O_5$. When the proteins were injected into the system (1800 s), flowing through sensor surfaces, a rapid increase of $\Delta M$ and a significant decrease of $\Delta f_s$ can be observed. Subsequently, for both groups and proteins, $\Delta M$ values were gradually increased over time, while $\Delta f_s$ showed the opposite behavior. Interestingly, in fibrinogen adsorption tests, it was observed that the $Ta_2O_5$ group reached the maximum value of $\Delta M$ (as appointed by the black arrows in the graph) more quickly when compared with the Ti group, indicating that the $Ta_2O_5$ film may have a rapid response of fibrinogen adsorption when compared with Ti. This behavior corroborates the quantitative results shown in Table 4, wherein the $Ta_2O_5$ group presented a tendency to higher adsorption rate values. In addition, the effective mass gain ($\Delta M$ - mass loss) results indicate that such values would provide good biological performance for $Ta_2O_5$-treated surfaces, as shown in the following cellular results.

### 3.5. Cell metabolism and morphology

An appropriate cellular response to implanted surfaces is crucial for tissue integration [59]. Therefore, in the current study, we carried out the MTT assay to determine the impact of $Ta_2O_5$-modified cpTi surfaces on cell morphology and metabolism. The absorbance of formazan crystals produced by MC3T3-E1 cells after 1, 2, and 4 days of culturing is presented in Fig. 10. In general, data analysis showed that both groups (control and experimental) presented an increased mitochondrial metabolism over time, suggesting a non-cytotoxic effect, with the $Ta_2O_5$-treated group featuring an increased metabolism at day 2.

If cells are to proliferate and differentiate, adhesion to surfaces is crucial [60,61]. Here, we investigated the impact of $Ta_2O_5$-modified cpTi surfaces on MC3T3-E1 cell adhesion and spreading after 1, 2, and 4 days, using SEM and confocal analysis (Figs. 11 and 12). According to previous literature, shapes, widths, and sizes of diverse nanoscale patterns can considerably influence cell adhesion, morphology, and differentiation [43]. In the current investigation, morphological analyses demonstrated that the $Ta_2O_5$-treated group displayed a well-defined and organized cytoskeleton, reflecting normal behavior [36] and well-spread morphologies when compared with those of the cpTi substrate at all experimental periods. In addition, significantly more filopodia extensions were found for MC3T3-E1 cells cultured on $Ta_2O_5$ substrates, indicating that $Ta_2O_5$-coated samples positively affected important cellular properties *in vitro*, including adhesion, spreading, and migration.

### 3.6. Mineralization potential

Next, we hypothesized that $Ta_2O_5$-modified surfaces would affect MC3T3-E1 cell differentiation and improve mineral nodule formation *in vitro*. To test our hypothesis, we cultured cells on our control and experimental discs under osteogenic and non-osteogenic (control) conditions and carried out the AR-S assays to assess mineral nodule formation quantitatively at 4, 7, and 14 days (Fig. 13). Intragroup analysis demonstrated a significant increase in mineralization for both surfaces

**Table 4**
Mean and (standard deviation) values of albumin and fibrinogen adsorption kinetics parameters obtained from EQCM analysis.

| Protein | Group | $\Delta M$ (μg) | Adsorption rate (ng/s) | Mass loss (μg) | Effective mass gain ($\Delta M$ - Mass loss) (μg) |
|---|---|---|---|---|---|
| Albumin | Ti | 0.12 (0.08) | 0.01 (0.00) | 0.01 (0.01) | 0.10 (0.06) |
| | $Ta_2O_5$ | 0.12 (0.02) | 0.54 (0.72) | 0.04 (0.04) | 0.07 (0.05) |
| Fibrinogen | Ti | 0.14 (0.01) | 0.02 (0.01) | 0.01 (0.01) | 0.13 (0.02) |
| | $Ta_2O_5$ | 0.12 (0.02) | 0.03 (0.02) | 0.01 (0.01) | 0.11 (0.02) |

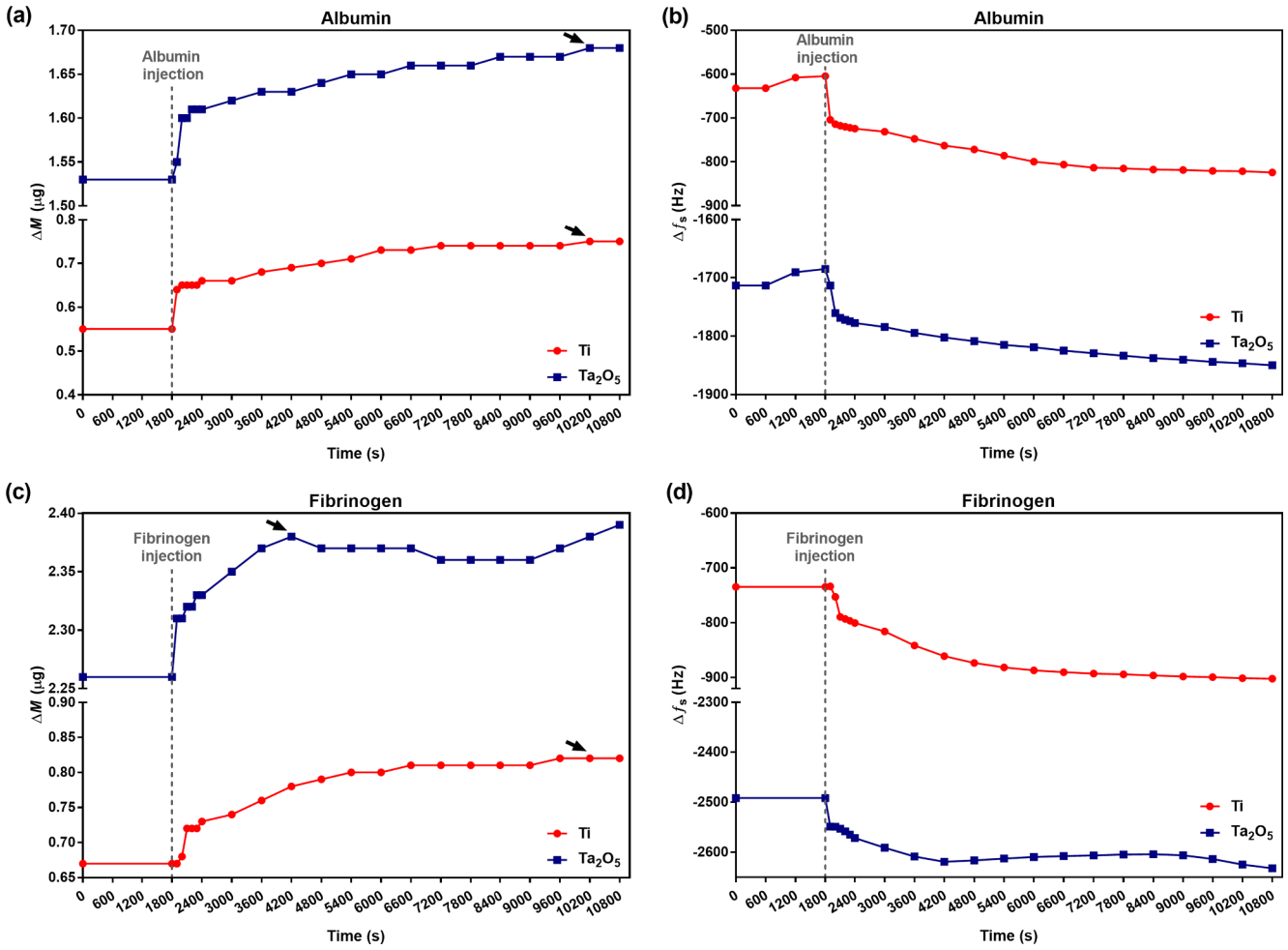


**Fig. 9.** Changes in $\Delta f_s$ and $\Delta M$ as a function of time during the adsorption processes of (a-b) albumin and (c-d) fibrinogen on quartz crystal sensors covered with Ti (red curves) and treated with $Ta_2O_5$ (blue curves). Black arrows indicate the maximum $\Delta M$ value for each group.

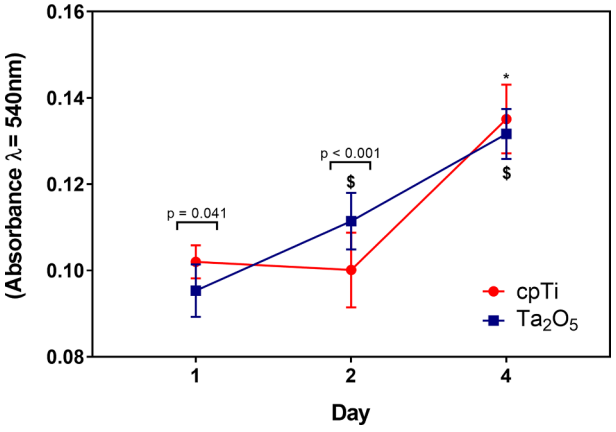


**Fig. 10.** MTT assay. Absorbance is expressed as a measure of cell metabolism for MC3T3-E1 cells cultured on control cpTi (untreated; red curve) and $Ta_2O_5$-modified surfaces (blue curve). * indicates intragroup differences (vs day 1) for cpTi, and $ indicates intragroup differences (vs day 1) for $Ta_2O_5$ film. Intergroup differences (cpTi vs $Ta_2O_5$) within the same day are illustrated by the p-value.

over time under osteogenic conditions at days 7 and 14. Intriguingly, intergroup comparisons showed that $Ta_2O_5$-modified surfaces displayed increased calcium levels under non-osteogenic conditions at days 7 and 14, and at day 14 under osteogenic differentiation. Altogether, these findings demonstrate that $Ta_2O_5$ films have the potential to enhance the differentiation of osteoblastic precursors cultured on cpTi discs.

### 3.7. Gene expression

For further investigation of the impact of $Ta_2O_5$-modified surfaces on the differentiation of osteoblastic precursor cells (MC3T3-E1), in the current study the expression of classic osteoblastic differentiation markers (including *Runx-2, Ocn, Alpl,* and *Col-1*) was quantitatively assessed (Fig. 14). Data analysis showed that transcript levels were increased by osteogenic conditions, except for *Runx-2* and *Alpl* at day 3. In addition, the findings of the current investigation demonstrated that $Ta_2O_5$-treated surfaces have the potential to modulate the expression of key markers of osteoblastic differentiation. Under osteogenic induction, fold change for *Runx-2* was significantly increased by $Ta_2O_5$-treated surfaces as early as 24 h after osteogenic induction, at days 2 and 3 for *Ocn* and at day 3 for *Col-1,* as compared with the cpTi group. In contrast to the cpTi group, at day 3, $Ta_2O_5$-modified surfaces resulted in decreased expression of *Runx-2* and *Alpl* in MC3T3-E1 cells under differentiation. Intergroup analysis further demonstrated that, at days 2 and 3, $Ta_2O_5$-modified surfaces led to increased changes for *Ocn* transcript levels as compared with cpTi under osteogenic conditions, whereas *Col-1* fold change was increased at day 3. Taken together, these findings suggest that $Ta_2O_5$ films have the potential to anticipate osteoblast precursor cell differentiation and, therefore, support the hypothesis that $Ta_2O_5$ films functionally affect markers of osteoblastic differentiation, leading to increased mineralization *in vitro*.

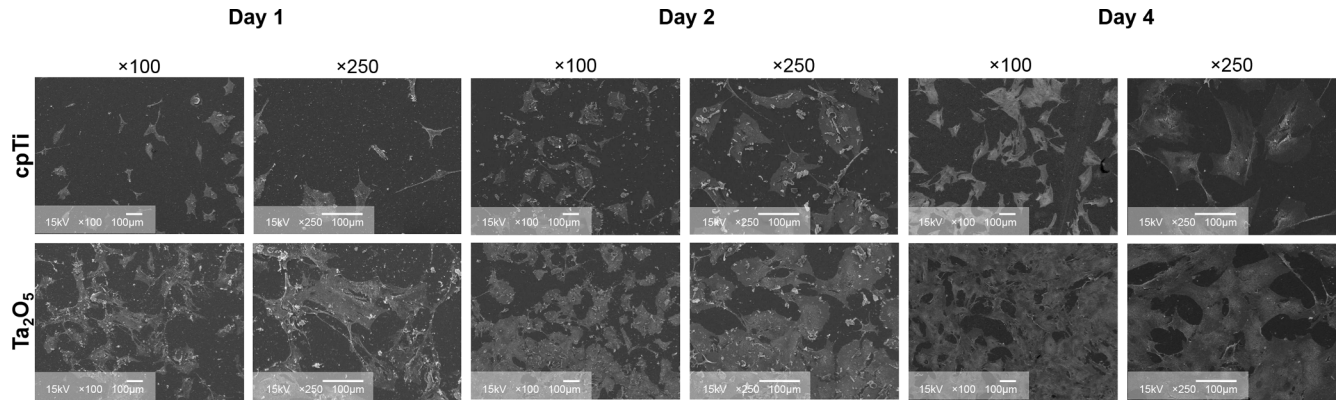


**Fig. 11.** Representative SEM images of MC3T3E-1 cells cultured on control cpTi and $Ta_2O_5$-modified surfaces after 1 day, 2 days, and 4 days. (scale bar = 100 μm).

### 3.8. Surface bioactivity

To evaluate the osteoconductive response of the $Ta_2O_5$-treated surface and its potential for use as a biomaterial, we carried out a bioactivity test in SBF. Fig. 15 shows the XRD results of the samples immersed in SBF after 14 days. The $Ta_2O_5$ group presented a low-intensity diffraction peak corresponding to hydroxyapatite (HA) at 55.88° (ICDD card number 532741) and peaks related to $Ta_2O_5$ as mentioned previously in the characterization results. Depending on the degree of crystallinity in the tantalum oxide films, substitution of carbonate may occur within the apatite structure, in two distinct ways: in the OH-site as an "A-type' substitution or in the $PO_4$-site as a "B-type" substitution. Indeed, in the "B-type", amorphous carbonate can be incorporated into the structure of the hydroxyapatite, which can reduce the degree of crystallinity of the apatite, as observed by Almeida Alves *et al.* (2016) [62]. In contrast, the cpTi group showed diffraction peaks related only to metallic Ti, implying that no calcium phosphate is detected by XRD.

### 3.9. Practical implications

Here, we proposed a surface modification of Ti with a β-$Ta_2O_5$ thin film to maintain the key physical properties of the bulk Ti material while modifying only its external surface. Such a modification controls

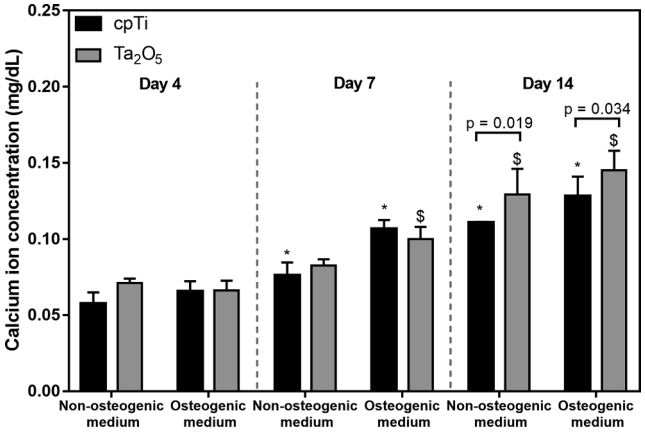


**Fig. 13.** Calcium ion concentrations for control and $Ta_2O_5$-modified surfaces. MC3T3-E1 cells were plated onto uncoated cpTi and $Ta_2O_5$-coated discs and cultured or not under osteogenic conditions for 4, 7, and 14 days. * indicates intragroup differences (vs day 4) for cpTi, and $ indicates intragroup differences (vs day 4) for $Ta_2O_5$ film in non-osteogenic or osteogenic medium conditions separately. Intergroup differences (cpTi vs $Ta_2O_5$) within the same day are illustrated by the p-value.

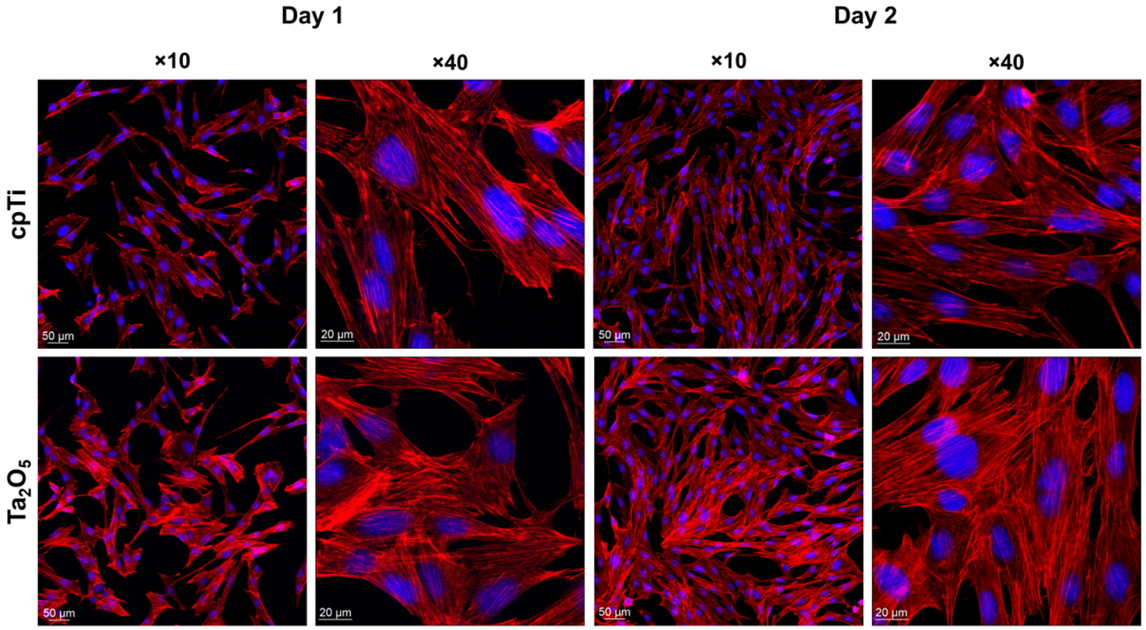


**Fig. 12.** Representative confocal images of MC3T3E-1 cells cultured on control cpTi and $Ta_2O_5$-modified surfaces after 1 and 2 days. Cell nuclei are stained in blue and the cell cytoskeleton in red.

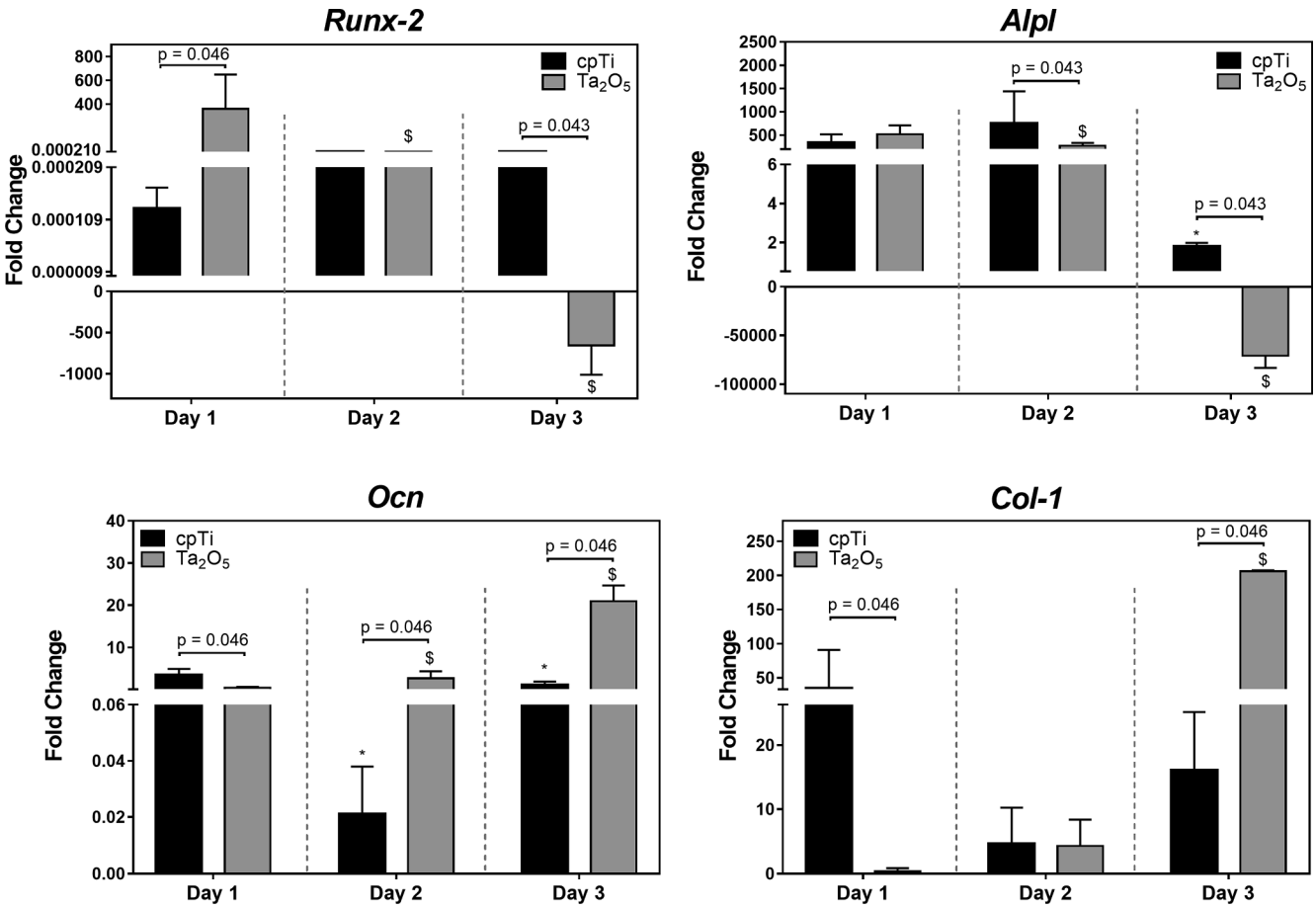


**Fig. 14.** Bar graphs illustrating fold change (osteogenic/non-osteogenic conditions) of osteogenic markers, including *Runx-2, Alpl, Ocn,* and *Col-1,* in MC3T3-E1 cells cultured on control cpTi and $Ta_2O_5$-modified surfaces. * indicates intragroup differences (vs day 1) for cpTi, and $ indicates intragroup differences (vs day 1) for $Ta_2O_5$ film. Intergroup differences (cpTi vs $Ta_2O_5$) within the same day are illustrated by the p-value.

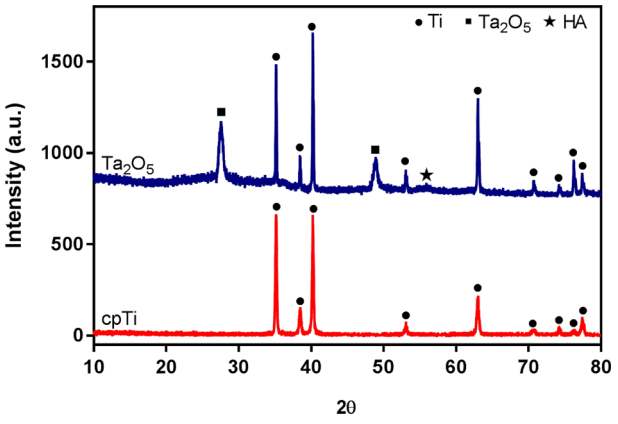


**Fig. 15.** XRD patterns of control cpTi (red pattern) and $Ta_2O_5$ (blue pattern) surfaces after 14 days of immersion in SBF at 37 °C.

the surface properties (such as roughness and surface energy) and, consequently, fosters the biological performance and prevents implant degradation in the biological environment. We show that the $Ta_2O_5$ film is able to protect cpTi against corrosion and, at the same time, enhance its cytocompatibility and bioactivity. The results obtained in this study demonstrate that the addition of a $Ta_2O_5$ film may be a forthcoming surface treatment feature to trigger the superior long-term stability of Ti implants. However, further studies are required to evaluate the interaction of such developed surface with living tissues.

## 4. Conclusions

We successfully developed a strategy to deposit a crystalline β-$Ta_2O_5$ thin film onto a cpTi surface by utilizing a magnetron sputtering technique. $Ta_2O_5$-treated surfaces exhibited greater roughness and hydrophilicity compared to untreated cpTi discs (control). Enhanced electrochemical stability in simulated body fluid was noted for $Ta_2O_5$-treated surfaces wherein higher values of charge transfer resistance, nobler corrosion potential, and lower values of capacitance, corrosion current density, and corrosion rate were observed. Also, pre-osteoblastic cell culture assays (MC3T3-E1 cells) demonstrated that $Ta_2O_5$-treated discs featured greater *in vitro* mineral nodule formation and increased mRNA levels of runt-related transcription factor 2 *(Runx-2)*, osteocalcin *(Ocn),* and collagen-1 *(Col-1)*. The findings of the current investigation indicate that modification of cpTi surfaces with β-$Ta_2O_5$ films emerges as a viable and promising strategy to enhance dental implant electrochemical stability, improving its surface properties and biological performance.

## CRediT authorship contribution statement

**Thamara Beline:** Conceptualization, Methodology, Validation, Formal analysis, Investigation, Data curation, Writing - original draft, Visualization. **Amanda B. Almeida:** Methodology, Validation, Formal analysis, Writing - review & editing. **Nilton F. Azevedo Neto:** Methodology, Writing - review & editing. **Adaias O. Matos:** Investigation, Writing - review & editing. **Antônio P. Ricomini-Filho:** Methodology, Writing - review & editing. **Cortino Sukotjo:**

Investigation, Resources, Writing - review & editing. **Paul J.M. Smeets:** Investigation, Resources, Writing - review & editing. **José H.D. Silva:** Conceptualization, Methodology, Resources, Writing - review & editing, Funding acquisition. **Francisco H. Nociti:** Conceptualization, Methodology, Resources, Writing - review & editing. **Valentim A.R. Barão:** Conceptualization, Methodology, Formal analysis, Resources, Writing - review & editing, Supervision, Project administration, Funding acquisition.

## Declaration of Competing Interest

The authors declare that they have no known competing financial interests or personal relationships that could have appeared to influence the work reported in this paper.

## Acknowledgments

This study was supported by the São Paulo State Research Foundation (FAPESP), Brazil (grant numbers 2016/07269-3, 2016/11470-6 and 2017/18916-2), and in part by the Coordenação de Aperfeiçoamento de Pessoal de Nível Superior - Brasil (CAPES) - Finance code 001. The authors express their gratitude to the Brazilian Nanotechnology National Laboratory (LNNano) for the use of XRD, AFM, and XPS facilities and to the Microscopy Laboratory of Araraquara School of Dentistry (UNESP) for the use of Confocal Fluorescence Microscopy facilities. Additionally, this work made use of the EPIC facility of Northwestern University's NUANCE Center, which has received support from the Soft and Hybrid Nanotechnology Experimental (SHyNE) Resource (NSF ECCS-1542205); the MRSEC program (NSF DMR-1720139) at the Materials Research Center; the International Institute for Nanotechnology (IIN); the Keck Foundation; and the State of Illinois, through the IIN.

## Appendix A. Supplementary material

Supplementary data to this article can be found online at https://doi.org/10.1016/j.apsusc.2020.146326.

## References

[1] S. Prasad, M. Ehrensberger, M.P. Gibson, H. Kim, E.A. Monaco, Biomaterial properties of titanium in dentistry, J. Oral Biosci. 57 (2015) 192–199, https://doi.org/10.1016/j.job.2015.08.001.
[2] N. Cabrera, N. Mott, Theory of the oxidation of metals, Rep. Prog. Phys. 12 (1949) 163–184.
[3] L. Wang, H. Yu, K. Wang, H. Xu, S. Wang, D. Sun, Local fine structural insight into mechanism of electrochemical passivation of titanium, ACS Appl. Mater. Interf. (2016), https://doi.org/10.1021/acsami.6b05080.
[4] D. Cadosch, E. Chan, O.P. Gautschi, L. Filgueira, Metal is not inert: role of metal ions released by biocorrosion in aseptic loosening - current concepts, J. Biomed. Mater. Res. A. 91 (2009) 1252–1262, https://doi.org/10.1002/jbm.a.32625.
[5] R. Bhola, S.M. Bhola, B. Mishra, D.L. Olson, Corrosion in titanium dental implants/prostheses - a review, Trends Biomater. Artif. Organs. 25 (2011) 34–46.
[6] T. Beline, I. da S.V. Marques, A.O. Matos, E.S. Ogawa, A.P. Ricomini-Filho, E.C. Rangel, N.C. da Cruz, C. Sukotjo, M.T. Mathew, R. Landers, R.L.X. Consani, M.F. Mesquita, V.A.R. Barão, Production of a biofunctional titanium surface using plasma electrolytic oxidation and glow-discharge plasma for biomedical applications, Biointerphases 11 (1) (2016) 011013, https://doi.org/10.1116/1.4944061.
[7] M.T. Mathew, V.A. Barão, J.C.C. Yuan, W.G. Assunção, C. Sukotjo, M.A. Wimmer, What is the role of lipopolysaccharide on the tribocorrosive behavior of titanium? J. Mech. Behav. Biomed. Mater. 8 (2012) 71–85, https://doi.org/10.1016/j.jmbbm.2011.11.004.
[8] M. Nakagawa, S. Matsuya, T. Shiraishi, M. Ohta, Effect of fluoride concentration and pH on corrosion behavior of titanium for dental use, J. Dent. Res. 78 (1999) 1568–1572, https://doi.org/10.1177/00220345990780091201.
[9] T. Beline, C.S. Garcia, E.S. Ogawa, I.S.V. Marques, A.O. Matos, C. Sukotjo, M.T. Mathew, M.F. Mesquita, R.X. Consani, V.A.R. Barão, Surface treatment influences electrochemical stability of cpTi exposed to mouthwashes, Mater. Sci. Eng. C. 59 (2016) 1079–1088, https://doi.org/10.1016/j.msec.2015.11.045.
[10] D. Royhman, X. Dominguez-Benetton, J.C.C. Yuan, T. Shokuhfar, C. Takoudis, M.T. Mathew, C. Sukotjo, The role of nicotine in the corrosive behavior of a Ti-6Al-4V dental implant, Clin. Implant Dent. Relat. Res. 17 (2015) 352–363, https://doi.org/10.1111/cid.12239.
[11] V.A. Barao, M.T. Mathew, W.G. Assunção, J.C. Yuan, M.A. Wimmer, C. Sukotjo, The role of lipopolysaccharide on the electrochemical behavior of titanium, J. Dent. Res. 90 (2011) 613–618, https://doi.org/10.1177/0022034510396880.
[12] S. Sridhar, T.G. Wilson, K.L. Palmer, P. Valderrama, M.T. Mathew, S. Prasad, M. Jacobs, I.M. Gindri, D.C. Rodrigues, In vitro investigation of the effect of oral bacteria in the surface oxidation of dental implants, Clin. Implant Dent. Relat. Res. 17 (2015), https://doi.org/10.1111/cid.12285.
[13] S.M. Zhang, J. Qiu, F. Tian, X.K. Guo, F.Q. Zhang, Q.F. Huang, Corrosion behavior of pure titanium in the presence of actinomyces naeslundii, J. Mater. Sci. Mater. Med. 24 (2013) 1229–1237, https://doi.org/10.1007/s10856-013-4888-3.
[14] J. Cohen, Current concepts review. corrosion of metal orthopaedic implants, J. Bone Joint Surg. Am. 80 (1998) 1554.
[15] L.M. Safioti, G.A. Kotsakis, A.E. Pozhitkov, W.O. Chung, D.M. Daubert, Increased levels of dissolved titanium are associated with peri-implantitis – a case-control study, J. Periodontol. (2016) 1–12.
[16] N. Tagger Green, E.E. Machtei, J. Horwitz, M. Peled, Fracture of dental implants: literature review and report of a case, Implant Dent. 11 (2002) 137–143, https://doi.org/10.1097/01.ID.0000015066.39485.E5.
[17] M.D. Bermúdez, F.J. Carrión, G. Martínez-Nicolás, R. López, Erosion-corrosion of stainless steels, titanium, tantalum and zirconium, Wear (2005), https://doi.org/10.1016/j.wear.2004.09.023.
[18] V.K. Balla, S. Banerjee, S. Bose, A. Bandyopadhyay, Direct laser processing of a tantalum coating on titanium for bone replacement structures, Acta Biomater. 6 (2010) 2329–2334, https://doi.org/10.1016/j.actbio.2009.11.021.
[19] J. Xu, X. Ke Bao, T. Fu, Y. Lyu, P. Munroe, Z.-H. Xie, In vitro biocompatibility of a nanocrystalline β-Ta2O5 coating for orthopaedic implants, Ceram. Int. 44 (2018) 4660–4675, https://doi.org/10.1016/j.ceramint.2017.12.040.
[20] P. Sochacka, A. Miklaszewski, M. Jurczyk, P. Pecyna, M. Ratajczak, M. Gajecka, M.U. Jurczyk, Effect of hydroxyapatite and Ag, Ta2O5 or CeO2 addition on the properties of ultrafine-grained Ti31Mo alloy, J. Alloys Compd. 823 (2020) 153749, , https://doi.org/10.1016/j.jallcom.2020.153749.
[21] H. Yu, S. Zhu, X. Yang, X. Wang, H. Sun, M. Huo, Synthesis of coral-like tantalum oxide films via anodization in mixed organic-inorganic electrolytes, PLoS One. 8 (2013) e66447, , https://doi.org/10.1371/journal.pone.0066447.
[22] G. Xu, X. Shen, Y. Hu, P. Ma, K. Cai, Fabrication of tantalum oxide layers onto titanium substrates for improved corrosion resistance and cytocompatibility, Surf. Coatings Technol. 272 (2015) 58–65, https://doi.org/10.1016/j.surfcoat.2015.04.024.
[23] H. Zhang, H. Tang, T.M. Yue, Fabrication of Ta2O5 reinforced Ta-based coatings on ta substrates by laser cladding, Int. J. Metall. Mater. Eng. 4 (2018), https://doi.org/10.15344/2455-2372/2018/140.
[24] Y.S. Sun, J.H. Chang, H.H. Huang, Corrosion resistance and biocompatibility of titanium surface coated with amorphous tantalum pentoxide, Thin Solid Films. 528 (2013) 130–135, https://doi.org/10.1016/j.tsf.2012.06.088.
[25] I. Baía, M. Quintela, L. Mendes, P. Nunes, R. Martins, Performances exhibited by large area ITO layers produced by r.f. magnetron sputtering, Thin Solid Films. 337 (1999) 171–175, https://doi.org/10.1016/S0040-6090(98)01393-5.
[26] J. Alami, S. Bolz, K. Sarakinos, High power pulsed magnetron sputtering: Fundamentals and applications, J. Alloys Compd. 483 (2009) 530–534, https://doi.org/10.1016/j.jallcom.2008.08.104.
[27] T. Beline, J.H.D. da Silva, A.O. Matos, N.F. Azevedo Neto, A.B. de Almeida, F.H. Nociti Júnior, D.M.G. Leite, E.C. Rangel, V.A.R. Barão, Tailoring the synthesis of tantalum-based thin films for biomedical application: characterization and biological response, Mater. Sci. Eng. C. 101 (2019) 111–119, https://doi.org/10.1016/j.msec.2019.03.072.
[28] H.N. Pantaroto, K.P. Amorim, J. Matozinho Cordeiro, J.G.S. Souza, A.P. Ricomini-Filho, E.C. Rangel, A.L.R. Ribeiro, L.G. Vaz, V.A.R. Barão, Proteome analysis of the salivary pellicle formed on titanium alloys containing niobium and zirconium, Biofouling. 35 (2019) 173–186, https://doi.org/10.1080/08927014.2019.1580360.
[29] A.L.J. Pereira, L. Gracia, A. Beltrán, P.N. Lisboa-Filho, J.H.D. Da Silva, J. Andrés, Structural and electronic effects of incorporating Mn in TiO2films grown by sputtering: anatase versus Rutile, J. Phys. Chem. C. 116 (2012) 8753–8762, https://doi.org/10.1021/jp210682d.
[30] E.C. Combe, B.A. Owen, J.S. Hodges, A protocol for determining the surface free energy of dental materials, Dent. Mater. 20 (2004) 262–268, https://doi.org/10.1016/S0109-5641(03)00102-7.
[31] L. Müller, F.A. Müller, Preparation of SBF with different HCO3- content and its influence on the composition of biomimetic apatites, Acta Biomater. 2 (2006) 181–189, https://doi.org/10.1016/j.actbio.2005.11.001.
[32] X. Lou, P.M. Singh, Phase angle analysis for stress corrosion cracking of carbon steel in fuel-grade ethanol: Experiments and simulation, Electrochim. Acta. 56 (2011) 1835–1847, https://doi.org/10.1016/j.electacta.2010.07.024.
[33] V.A.R. Barao, M.T. Mathew, W.G. Assuncao, J.C.-C. Yuan, M.A. Wimmer, C. Sukotjo, Stability of cp-Ti and Ti-6Al-4V alloy for dental implants as a function of saliva pH - an electrochemical study, Clin. Oral Implants Res. 23 (2012) 1055–1062, https://doi.org/10.1111/j.1600-0501.2011.02265.x.
[34] V.A.R. Barão, A.P. Ricomini-Filho, L.P. Faverani, A.A. Del Bel Cury, C. Sukotjo, D.R. Monteiro, J.C.C. Yuan, M.T. Mathew, R.C. Do Amaral, M.F. Mesquita, W.J. Da Silva, W.G. Assunção, The role of nicotine, cotinine and caffeine on the electrochemical behavior and bacterial colonization to cp-Ti, Mater. Sci. Eng. C. 56 (2015) 114–124, https://doi.org/10.1016/j.msec.2015.06.026.
[35] G. Sauerbrey, The use of quartz oscillators for weighing thin layers and for microweighing, Zeitschrift Für Phys. 155 (1959) 206–222, https://doi.org/10.1007/BF01337937.
[36] I. da S.V. Marques, M.F. Alfaro, M.T. Saito, N.C. da Cruz, C. Takoudis, R. Landers,

M.F. Mesquita, F.H. Nociti Junior, M.T. Mathew, C. Sukotjo, V.A.R. Barão, Biomimetic coatings enhance tribocorrosion behavior and cell responses of commercially pure titanium surfaces, Biointerphases 11 (3) (2016) 31008, https://doi.org/10.1116/1.4960654.

[37] A.O. Matos, A.P. Ricomini-Filho, T. Beline, E.S. Ogawa, B.E. Costa-Oliveira, A.B. de Almeida, F.H. Nociti Junior, E.C. Rangel, N.C. da Cruz, C. Sukotjo, M.T. Mathew, V.A.R. Barão, Three-species biofilm model onto plasma-treated titanium implant surface, Colloids Surf. B Biointerf. 152 (2017) 354–366, https://doi.org/10.1016/j.colsurfb.2017.01.035.

[38] T.L. Rodrigues, B.L. Foster, K.G. Silverio, L. Martins, M.Z. Casati, E.A. Sallum, M.J. Somerman, F.H. Nociti, Hypophosphatasia-associated deficiencies in mineralization and gene expression in cultured dental pulp cells obtained from human teeth, J. Endod. 38 (2012) 907–912, https://doi.org/10.1016/j.joen.2012.02.008.

[39] T. Kokubo, H. Takadama, How useful is SBF in predicting in vivo bone bioactivity? Biomaterials. 27 (2006) 2907–2915, https://doi.org/10.1016/j.biomaterials.2006.01.017.

[40] M. Birkholz, Thin Film Analysis by X-Ray Scattering, first ed., Wiley-VCH, Frankfurt, Germany, 2006.

[41] K. Lehovec, Lattice structure of β-Ta2O5, J. Less-Common Met. 7 (1964) 397–410, https://doi.org/10.1016/0022-5088(64)90036-0.

[42] M.H. Ding, B.L. Wang, L. Li, Y.F. Zheng, A study of TaxC1 − x coatings deposited on biomedical 316L stainless steel by radio-frequency magnetron sputtering, Appl. Surf. Sci. 257 (2010) 696–703, https://doi.org/10.1016/j.apsusc.2010.07.026.

[43] H. Jeon, C.G. Simon, G. Kim, A mini-review: cell response to microscale, nanoscale, and hierarchical patterning of surface structure, J. Biomed. Mater. Res. Part B Appl. Biomater. 102 (2014) 1580–1594, https://doi.org/10.1002/jbm.b.33158.

[44] A. Ranella, M. Barberoglou, S. Bakogianni, C. Fotakis, E. Stratakis, Tuning cell adhesion by controlling the roughness and wettability of 3D micro/nano silicon structures, Acta Biomater. 6 (2010) 2711–2720, https://doi.org/10.1016/j.actbio.2010.01.016.

[45] A. Aminian, B. Shirzadi, Z. Azizi, K. Maedler, E. Volkmann, N. Hildebrand, M. Maas, L. Treccani, K. Rezwan, Enhanced cell adhesion on bioinert ceramics mediated by the osteogenic cell membrane enzyme alkaline phosphatase, Mater. Sci. Eng. C. 69 (2016) 184–194, https://doi.org/10.1016/j.msec.2016.06.056.

[46] W. Ren, Z. Ai, F. Jia, L. Zhang, X. Fan, Z. Zou, Low temperature preparation and visible light photocatalytic activity of mesoporous carbon-doped crystalline TiO2, Appl. Catal. B Environ. 69 (2007) 138–144, https://doi.org/10.1016/j.apcatb.2006.06.015.

[47] J.-H. Kim, S. Lee, H.-S. Im, The effect of target density and its morphology on TiO2 thin films grown on Si(100) by PLD, Appl. Surf. Sci. 151 (1999) 6–16, https://doi.org/10.1016/S0169-4332(99)00269-X.

[48] A.C. Hee, Y. Zhao, S.S. Jamali, P.J. Martin, A. Bendavid, H. Peng, X. Cheng, Corrosion behaviour and microstructure of tantalum film on Ti6Al4V substrate by filtered cathodic vacuum arc deposition, Thin Solid Films. 636 (2017) 54–62, https://doi.org/10.1016/j.tsf.2017.05.030.

[49] A.C. Hee, H. Cao, Y. Zhao, S.S. Jamali, A. Bendavid, P.J. Martin, Cytocompatible tantalum films on Ti6Al4V substrate by filtered cathodic vacuum arc deposition, Bioelectrochemistry 122 (2018) 32–39, https://doi.org/10.1016/j.bioelechem.2018.02.006.

[50] Y. Cheng, W. Cai, H.T. Li, Y.F. Zheng, L.C. Zhao, Surface characteristics and corrosion resistance properties of TiNi shape memory alloy coated with Ta, Surf. Coatings Technol. 186 (2004) 346–352, https://doi.org/10.1016/j.surfcoat.2004.01.012.

[51] M. Textor, L. Ruiz, R. Hofer, A. Rossi, K. Feldman, G. Hähner, N.D. Spencer, Structural chemistry of self-assembled monolayers of octadecylphosphoric acid on tantalum oxide surfaces, Langmuir 16 (2000) 3257–3271, https://doi.org/10.1021/la990941t.

[52] T. Fu, Z. Zhan, L. Zhang, Y. Yang, Z. Liu, J. Liu, L. Li, X. Yu, Effect of surface mechanical attrition treatment on corrosion resistance of commercial pure titanium, Surf. Coatings Technol. 280 (2015) 129–135, https://doi.org/10.1016/j.surfcoat.2015.08.041.

[53] A.C. Hee, Y. Zhao, S.S. Jamali, A. Bendavid, P.J. Martin, H. Guo, Characterization of tantalum and tantalum nitride films on Ti6Al4V substrate prepared by filtered cathodic vacuum arc deposition for biomedical applications, Surf. Coatings Technol. 365 (2019) 24–32, https://doi.org/10.1016/j.surfcoat.2018.05.007.

[54] T. Beline, A.J. Vechiato Filho, A.G. Wee, C. Sukotjo, D.M. dos Santos, T.B. Brandão, V.A.R. Barão, Initial investigation of the corrosion stability of craniofacial implants, J. Prosthet. Dent. 119 (2018) 185–192, https://doi.org/10.1016/j.prosdent.2017.02.015.

[55] P. Silva-Bermudez, S.E. Rodil, An overview of protein adsorption on metal oxide coatings for biomedical implants, Surf. Coatings Technol. 233 (2013) 147–158, https://doi.org/10.1016/j.surfcoat.2013.04.028.

[56] M. Talha, Y. Ma, P. Kumar, Y. Lin, A. Singh, Role of protein adsorption in the bio corrosion of metallic implants – A review, Colloids Surf. B Biointerf. 176 (2019) 494–506, https://doi.org/10.1016/j.colsurfb.2019.01.038.

[57] C. Sperling, M. Fischer, M.F. Maitz, C. Werner, Blood coagulation on biomaterials requires the combination of distinct activation processes, Biomaterials 30 (2009) 4447–4456, https://doi.org/10.1016/j.biomaterials.2009.05.044.

[58] C. Werner, M.F. Maitz, C. Sperling, Current strategies towards hemocompatible coatings, J. Mater. Chem. 17 (2007) 3376, https://doi.org/10.1039/b703416b.

[59] C.J. Wilson, R.E. Clegg, D.I. Leavesley, M.J. Pearcy, Mediation of biomaterial-cell interactions by adsorbed proteins: a review, Tissue Eng. (2005), https://doi.org/10.1089/ten.2005.11.1.

[60] J.Y. Martin, Z. Schwartz, T.W. Hummert, D.M. Schraub, J. Simpson, J. Lankford, D.D. Dean, D.L. Cochran, B.D. Boyan, Effect of titanium surface roughness on proliferation, differentiation, and protein synthesis of human osteoblast-like cells (MG63), J. Biomed. Mater. Res. 29 (1995) 389–401, https://doi.org/10.1002/jbm.820290314.

[61] K.-D. Yun, Y. Yang, H.-P. Lim, G.-J. Oh, J.-T. Koh, I.-H. Bae, J. Kim, K.-M. Lee, S.-W. Park, Effect of nanotubular-micro-roughened titanium surface on cell response in vitro and osseointegration in vivo, Mater. Sci. Eng. C. 30 (2010) 27–33, https://doi.org/10.1016/j.msec.2009.08.004.

[62] C.F. Almeida Alves, A. Cavaleiro, S. Carvalho, Bioactivity response of Ta1-xOx coatings deposited by reactive DC magnetron sputtering, Mater. Sci. Eng. C. 58 (2016) 110–118, https://doi.org/10.1016/j.msec.2015.08.017.